Impact of Swell on the Marine Atmospheric Boundary Layer

V. N. KUDRYAVTSEV

Marine Hydrophysical Institute, Sevastopol, Ukraine, and Nansen Environmental and Remote Sensing Center, Bergen, Norway

V. K. MAKIN

Royal Netherlands Meteorological Institute (KNMI), De Bilt, Netherlands

(Manuscript received 28 February 2003, in final form 19 September 2003)

ABSTRACT

A model that describes the impact of swell on the marine atmospheric boundary layer is proposed. The model is based on the two-layer approximation of the boundary layer: the near-surface inner region and the outer region above. The swell-induced momentum and energy fluxes are confined within the inner region. Swell loses energy to the atmosphere and enhances the turbulent kinetic energy in the inner region. The transfer of momentum results in acceleration or deceleration of the airflow near the surface. Following-wind swell accelerates the flow, which for a very low wind results in a swell-driven wind. Opposite-wind swell decelerates the airflow, which for a steep swell could cause the reverse airflow. The sea drag in the case of opposite-wind swell is considerably enhanced as compared with the following-wind swell case. Cross-wind swell causes the rotation of the wind velocity vector with height, which leads to the deviation of the turbulent stress vector from the wind velocity vector. The impact of swell becomes more pronounced when the wind speed decreases or when the swell phase velocity increases. In fact, it is the wave age of the swell that characterizes the swell impact because the dimensionless wave-induced fluxes of energy and momentum are proportional to the wave age parameter. Both fluxes are also proportional to the swell slope so that the swell impact is stronger for a steeper swell. The model reproduces qualitatively and quantitatively the main experimental findings for the ocean swell: the impact of swell on the sea drag is very pronounced for opposite-wind swell, is less pronounced for cross-wind swell, and is only at low wind speeds.

1. Introduction

Experimental estimates of the sea drag coefficient demonstrate a large scatter within individual experiments and between different experiments. It is suggested that one of the reasons for such a large scatter could be the unsteady wind conditions and the variable sea state (Drennan et al. 1999). In the case of a developing wind sea, several studies have shown that the drag coefficient is dependent on wave age (e.g., Donelan et al. 1993; Maat et al. 1991; Smith et al. 1992). In terms of the Charnock parameter this dependence reads $z_0 g/u_*^2 \sim (u_*/C_p)^n$, where z_0 is the roughness scale, u_* is the friction velocity, g is the acceleration of gravity, C_p is the phase velocity at the peak of the wave spectra, and n is a positive exponent. Despite differences in the experimental estimate of n, measurements revealed the undoubted fact that the younger wind sea supports the larger sea drag. Makin and Kudryavtsev (2002) argued that the airflow separation from breaking dominant wind-generated waves is responsible for the observed enhancement of the sea drag in the young sea.

A young sea usually corresponds to the fetch- and/or duration-limited conditions. That is not typical for the open ocean. Mixed wind sea–swell or pure swell conditions are the most remarkable features of the open ocean. Yelland and Taylor (1996) found that in the open ocean at low wind speeds, the drag coefficient increases with a decrease in the wind speed. This rather rapid increase cannot be explained by the aerodynamically smooth conditions of the sea surface. The authors mentioned that during the ocean cruise, the wave field at low winds was always dominated by swell, and that it is very likely that the impact of swell on the atmosphere could result in a strong increase in the drag coefficient at low winds. Donelan et al. (1997) found a strong increase in the drag coefficient at low winds in the presence of swell traveling across or opposite to the wind. This finding was confirmed by Drennan et al. (1999), who also observed the enhanced sea drag under the same conditions. They concluded that much of the scatter in the drag coefficient could be attributed to the presence of swell. Guo-Larsen et al. (2003), using measurements from the Baltic Sea, have shown that the cross swell

Corresponding author address: Dr. V. K. Makin, KNMI, P.O. Box 201, 3730 AE De Bilt, Netherlands.
E-mail: makin@knmi.nl

enhances the sea drag as compared with the following-swell case and that the magnitude of the drag coefficient is increased with increasing the angle of swell propagation to the wind. However, no quantitative relations describing the impact of swell on the sea surface drag were proposed, nor were the physical mechanisms responsible for the impact revealed. Another related phenomenon is the occasional observations of the upward momentum transfer (e.g., Davidson and Frank 1973; Grachev and Fairall 2001), which is manifested in a wave-driven wind. Swell traveling faster than the wind transfers momentum to the atmosphere and accelerates the airflow close to the sea surface (Harris 1966; Smedman et al. 1999).

It should be clearly realized however that the reported impacts of swell on the atmospheric boundary layer can be attributed only with some certainty to waves. A possibility exists that mesoscale turbulent or convective motions in the marine atmospheric boundary layer, completely independent of swell, are entirely or predominantly responsible for the observed peculiarities. For example, it could be realized (Grachev and Fairall 2001, their Fig. 7) that the reported upward momentum transport assigned by authors to swell is mainly due to motions with frequency around 0.005 Hz. This points at mesoscale motions rather than at swell signature.

Low winds and the presence of swell are typical of tropical ocean regions, where the atmosphere accumulates heat and moisture and then transfers them to higher latitudes. In that respect the understanding of swell impact on the exchange processes at the air–sea interface is one of the key issues in climate research. In the present paper a model that describes the impact of swell on the marine atmospheric boundary layer (MABL) and, in particular, on the sea drag is proposed. The physical mechanism responsible for that impact is explained and quantitative estimates of the impact of swell on the momentum flux and the wind profile in the MABL at various wind swell conditions are given. It is shown that under certain conditions the impact of swell on the MABL can be dramatic.

2. Model

a. Governing equations

A neutrally stratified marine atmospheric boundary layer in the presence of swell is considered. Swell is characterized by the amplitude A, wavenumber K, and frequency Ω connected by the dispersion relation for waves on deep water. In the Cartesian coordinate system moving with the phase velocity of swell, $C = \Omega/K$, the x_1 axis aligned with the swell propagation direction, the x_2 axis parallel to the swell crest, and the x_3 axis directed upward, the sea surface displacement is

$$z(x_\alpha, t) = Ae^{iKx_1}. \quad (1)$$

Hereinafter only the real part of this or any other quantity is to be considered.

The wind and wave fields are assumed to be stationary and spatially homogeneous, and the wind direction is arbitrary with respect to the swell direction. Governing equations—describing the vertical structure of the one-dimensional averaged over the horizontal coordinates MABL above waves—are the momentum and the turbulent kinetic energy (TKE) conservation equations (e.g., Makin and Mastenbroek 1996). In the present study the equations are refined by rewriting them in a more convenient and widely used wave-following orthogonal coordinate system, which is defined in the appendix. Derivations of the equations are also given there.

The momentum and TKE conservation equations in the wave-following ξ_i-coordinate system [see (A14) and (A17)] are

$$\tau_\alpha^w(\varsigma) + \tau_\alpha(\varsigma) = \tau_{0\alpha} \quad \text{and} \quad (2)$$

$$\frac{\partial}{\partial\varsigma}F^t + \tau_\alpha\frac{\partial U_\alpha}{\partial\varsigma} + \overline{\tilde{\tau}_{ij}\frac{\partial\tilde{u}_i}{\partial\xi_j}} - \text{Diss} = 0, \quad (3)$$

where $\varsigma \equiv \xi_3$ is the vertical wave-following coordinate; $\alpha = 1, 2$; and $i, j = 1, 2, 3$. In addition, $\tau_\alpha^w(\varsigma)$ is the wave-induced momentum flux defined by (A13), $\tau_\alpha(\varsigma)$ is the turbulent shear stress, $\tau_{0\alpha}$ is the total shear stress in the MABL far away from the sea surface where the impact of waves on the stress is negligible, F^t is the vertical flux of the TKE, Diss is the viscous dissipation of the TKE, U_α is the mean wind velocity in the moving coordinate system related to $\overline{u}_\alpha$ in the fixed coordinate system as $U_1 = \overline{u}_1 - C$, and $U_2 = \overline{u}_2$. The momentum conservation equation (2) shows that the sum of the wave-induced and turbulent stress is constant over height. At the sea surface $\varsigma = \varsigma_0$ (where ς_0 is the roughness scale of the wavy surface) the wave-induced stress (form drag) is

$$\tau_{s1}^w = \overline{\tilde{p}_s z_1}, \quad (4)$$

where $\tau_{s1}^w \equiv \tau_1^w(\varsigma_0)$, $z_1 = \partial z/\partial x_1$ is the sea surface slope, and $\tilde{p}_s$ is the wave-induced pressure at the sea surface. The component of the form drag parallel to the wave crest is 0: $\tau_{s2}^w \equiv \tau_2^w(\varsigma_0) = 0$.

The TKE production due to the work of the wave-induced turbulent stress $\tilde{\tau}_{ij}$ against the shear in the wind velocity [third term on the left-hand side of (3)] can be expressed through the energy balance of the wave-induced motion (A15), where this term describes the sink of the wave-induced energy into the TKE [last term in (A15)]. With (A15) the TKE balance equation (3) is written as

$$\frac{\partial}{\partial\varsigma}(F^t + F^w) + (\tau_\alpha + \tau_\alpha^w)\frac{\partial U_\alpha}{\partial\varsigma} - \text{Diss} = 0, \quad (5)$$

where F^w is the vertical flux of the wave-induced energy. When the wave-induced momentum flux is comparable with the turbulent stress, that is, $\tau_\alpha^w \sim \tau_\alpha$, the effect of waves on the MABL could be significant. In this case the vertical flux of the TKE is much lower than the

vertical flux of the wave-induced energy. It is easy to show that in this case the ratio F^t/F^w is of order $F^t/F^w \sim u_*/C \ll 1$, where u_* is the friction velocity. Neglecting F^t in comparison with F^w and accounting for the momentum conservation equation (2) the TKE balance equation finally reads

$$\frac{\partial}{\partial \varsigma} F^w + \tau_{0\alpha} \frac{\partial U_\alpha}{\partial \varsigma} - \text{Diss} = 0. \tag{6}$$

According to (A16), the energy flux of the wave-induced motion at the sea surface is

$$F_s^w = -\overline{\tilde{p}_s \tilde{w}_s} + \overline{\tilde{u}_s \tilde{\tau}_{1s}} \tag{7}$$

$$= C\overline{\tilde{p}_s z_1} + \overline{\tilde{u}_s \tilde{\tau}_{1s}}, \tag{8}$$

where $\tilde{w}_s$ and $\tilde{u}_s$ are the vertical and horizontal components of the wave surface orbital velocity, and $\tilde{\tau}_{s1}$ is the wave-induced variation of the shear stress at the surface. This energy flux provides the growth or attenuation of the wave energy due to the work of normal and tangential stresses. Their relative contributions to the total wave growth rate depend on the wind and wave conditions and will be analyzed later.

To complete the problem a turbulence closure scheme has to be chosen. In the present study the simplest mixing length closure scheme is used. Assuming that the mixing length is proportional to the distance from the sea surface in the wave-following coordinate system, the turbulent shear stress and the TKE dissipation in Eqs. (2) and (6) are written as

$$\text{Diss} = \frac{b^{3/2}}{\kappa \varsigma}, \tag{9}$$

$$\tau_\alpha = k \frac{dU_\alpha}{d\varsigma}, \quad \text{and} \tag{10}$$

$$k = \kappa b^{1/2} \varsigma, \tag{11}$$

where b is the TKE and k is the turbulent eddy viscosity coefficient.

With (9)–(11) the governing equations of the problem are

$$\kappa b^{1/2} \varsigma \frac{dU_\alpha}{d\varsigma} = \tau_{0\alpha} - \tau_\alpha^w(\varsigma) \quad \text{and} \tag{12}$$

$$\frac{\partial}{\partial \varsigma} F^w + \tau_{0\alpha} \frac{\partial U_\alpha}{\partial \varsigma} - \frac{b^{3/2}}{\kappa \varsigma} = 0. \tag{13}$$

Using (12) the TKE balance equation (13) transforms into

$$b^2 = \tau_{0\alpha}[\tau_{0\alpha} - \tau_\alpha^w(\varsigma)] + \kappa \varsigma b^{1/2} \frac{\partial F^w(\varsigma)}{\partial \varsigma}. \tag{14}$$

If the vertical profiles of $\tau_\alpha^w(\varsigma)$ and $F^w(\varsigma)$ are known and the wind speed at the reference level h far away from the sea surface where the wave-induced fluxes are vanished is specified, the solution of Eqs. (12) and (14) gives a full description of the MABL: the drag coefficient, the wind velocity, the TKE profile, and so on. The solution of this problem for pure wind seas [the last term on the right-hand side of (14) can be then ignored] is given, for example, by Makin and Kudryavtsev (1999). In the presence of swell the last term on the right-hand side of (14) plays a significant role. It is easy to check that when the effects of waves on the atmospheric boundary layer are important (i.e., $\tau_{s1}^w \sim \tau_0$), the ratio of the second term to the first term on the right-hand side of (14) is of order $C/|U_l|$, where U_l is the wind speed at the height of the inner region defined in section 2b. Thus in the swell conditions ($C/|U_l| \gg 1$) the divergence of the wave energy [the last term on the right-hand side of (14)] is the dominant source of the TKE production.

b. Two-layer approximation

A two-layer approximation of the wave boundary layer is used for its description. According to the rapid distortion theory of turbulence applied to modeling the airflow above waves (e.g., Townsend 1972; Belcher and Hunt 1993; Belcher 1999; Kudryavtsev et al. 2001), numerical simulations of the airflow above waves based on Reynolds equations with a second-order turbulent stress closure scheme (e.g., Mastenbroek et al. 1996), direct numerical simulations (e.g., Sullivan et al. 2000), the wave-induced stress $\tau_\alpha^w(\varsigma)$, and the corresponding vertical flux of the wave-induced energy $F^w(\varsigma)$ are confined to a thin near-surface inner region (IR) characterized by the vertical scale l. They rapidly vanish outside the IR at $\varsigma > l$—in the outer region (OR). The scale of the IR can be defined as the vertical spreading height of the oscillation in the turbulent boundary layer caused by a wavy surface: $l^2 = k_l T_a$, where k_l is the effective eddy viscosity inside the IR, $T_a = 1/(K|U_l|)$ is the scale of the oscillation period, and $U_l = U_1(l) \equiv \overline{u}_1(l) - C$ is the wind velocity in a frame of reference moving with the wave phase speed at $\varsigma = l$. At arbitrary wind angle θ with respect to the wave propagation direction the eddy viscosity for the wave-induced turbulent stress variation is $k = (1 + \cos^2\theta)\kappa b^{1/2}\varsigma$. (Meirink et al. 2003). If we define k_l as the eddy viscosity at $\varsigma = l$ [i.e., $k_l = k(l)$] then the scale of the IR reads

$$Kl = (1 + \cos^2\theta)\kappa b^{1/2}/|U_l|. \tag{15}$$

At $\theta = 0°$ and $b^{1/2} = u_*$, (15) corresponds to the definition of the IR scale proposed by Belcher and Hunt (1993) and Cohen and Belcher (1999). The scales of the IR in the following-, cross-, and opposite-wind directions for the logarithmic wind velocity profile $|\overline{u}(\varsigma)| = u_*/\kappa \ln(\varsigma/\varsigma_0)$ are shown in Fig. 1 as a function of the inverse wave age parameter $|\overline{u}_\lambda|/C$, where $|\overline{u}_\lambda|$ is the wind speed at level $\varsigma = 2\pi/K$.

At the opposite- and cross-wind directions the dimensionless IR scale Kl is very small; its magnitude varies between 10^{-1} and 10^{-2}. At the following-wind direction the IR scale is also small for fast- and slow-

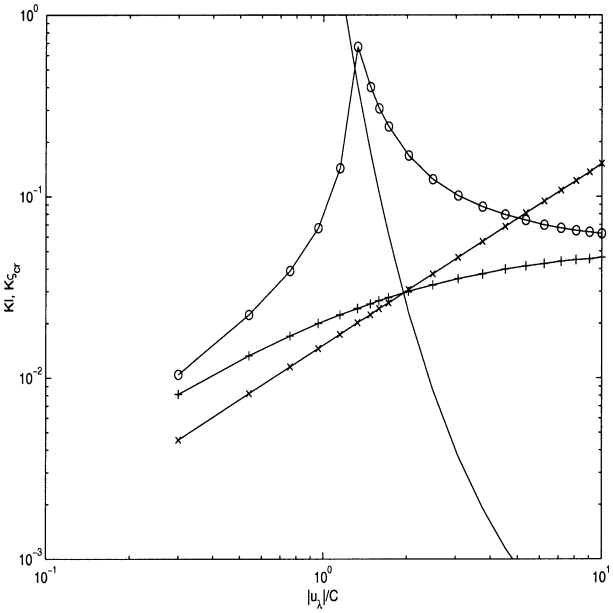

FIG. 1. Inner region depth Kl as a function of the inverse wave age parameter $|u_\lambda|/C$ for the swell-wind angle $\theta = 0°$ (solid line with open circles), 90° (solid line with crosses), and 180° (solid line with pluses). The height of the critical layer $K\varsigma_{cr}$ is shown by the solid line.

(with respect to the wind speed) propagating surface waves. When the phase velocity of the surface wave is close to the wind speed, the IR scale Kl increases to about 1. The height of the critical level $K\varsigma_{cr} = K\varsigma_0 \exp(\kappa C/u_*)$—the level where the wind speed is equal to the wave phase velocity in the case of a following-wind wave—is also shown in Fig. 1. In the range of the inverse wave age parameter $\overline{u}_\lambda/C > 1.5$, the height of the critical layer is well inside the IR. As was discussed by Belcher and Hunt (1993), Mastenbroek et al. (1996), and Kudryavtsev et al. (2001), this fact means that the dynamics of the critical layer is significantly affected by the turbulent stress and the nonseparated sheltering mechanism (Belcher and Hunt 1993) is the most plausible one in the description of the wave generation by the wind.

The concept of the IR allows for a significant simplification of the description of the wave boundary layer. According to Fig. 1, in most cases (except at $|\overline{u}_\lambda|/C \approx 1.5$ for the following-wind wave), the IR is a thin layer. Since $\tau^w_\alpha(\varsigma)$ and $F^w(\varsigma)$ are confined to the IR, a two-layer approximation of the wave boundary layer can be adopted. The two layers are the IR ($\varsigma < l$) and the OR ($\varsigma > l$). Inside the IR the wave-induced stress is constant over height and vanishes outside:

$$\tau^w_1(\varsigma) = \tau^w_{s1}, \quad \text{at } \varsigma_0 < \varsigma < l \quad \text{and} \tag{16}$$

$$\tau^w_1(\varsigma) = 0, \quad \text{at } \varsigma > l, \tag{17}$$

where τ^w_{s1} is the wave-induced stress at the sea surface (the form drag) defined by (4) (notice that component $\tau^w_{s2} = 0$). Correspondingly the profile of the vertical flux of the wave-induced energy has the following shape:

$$F^w(\varsigma) = F^w_s \frac{\ln(l/\varsigma)}{\ln(l/\varsigma_0)}, \quad \text{at } \varsigma_0 < \varsigma < l, \quad \text{and} \tag{18}$$

$$F^w(\varsigma) = 0, \quad \text{at } \varsigma > l, \tag{19}$$

where F^w_s is the energy flux at the sea surface defined by (8). The logarithmic shape of the F^w profile (18) follows from the wave-induced energy conservation equation (A15). The assumption that τ^w_1 is constant inside the IR dictates the logarithmic shape of the $F^w(\varsigma)$ profile.

With (16)–(19) the profile of the wind velocity and the TKE inside the IR ($\varsigma_0 < \varsigma < l$) follows from (12) and (14):

$$\overline{u}_\alpha(\varsigma) = \frac{\tau_{0\alpha} - \tau^w_{s\alpha}}{\kappa b^{1/2}} \ln\left(\frac{\varsigma}{\varsigma_0}\right) \quad \text{and} \tag{20}$$

$$b = \left[\tau_{0\alpha}(\tau_{0\alpha} - \tau^w_{s\alpha}) - \upsilon_*^2 \frac{F^w_s}{|U_l|}\right]^{1/2}, \tag{21}$$

where $\upsilon_* = |\tau_0 - \tau^w_s|^{1/2}$ is the friction velocity inside the IR and $|U_l| \equiv |\overline{u}_l(l) - C|$ is the wind velocity at $z = l$. In the OR $\varsigma > l$, the wind profile patches in to the wind velocity at the top of the IR and has a form

$$\overline{u}_\alpha(\varsigma) = \frac{\tau_{0\alpha}}{\kappa u_*} \ln\left(\frac{\varsigma}{l}\right) + \overline{u}_\alpha(l), \tag{22}$$

where $u_* = |\tau_0|^{1/2}$ is the friction velocity in the OR.

The resistance law relating the stress to the given wind velocity $u_{h\alpha}$ at the reference level h results from (20) and (22):

$$\frac{\tau_{0\alpha}}{u_*} = \frac{\kappa u_{h\alpha} + \tau^w_{s\alpha} b^{-1/2} \ln(l/\varsigma_0)}{\ln(h/l) + u_* b^{-1/2} \ln(l/\varsigma_0)}. \tag{23}$$

In the present study the aerodynamic roughness scale is specified through the modified Charnock relationship:

$$\varsigma_0 = a_1 \nu/\upsilon_* + a_2 \upsilon_*^2/g, \tag{24}$$

where $a_1 = 0.1$ and $a_2 = 0.012$ are constants, and ν is the molecular viscosity of the air. The parameterization of the roughness scale (24) is based on the IR friction velocity. The reason for this is that the momentum flux for very short wind waves parameterized by the second term on the right-hand side of (24) and the viscous surface stress parameterized by the first term on the right-hand side of (24), are both functions of the friction velocity in the IR rather than in the OR.

c. Parameterization of the form drag and wave energy flux at the surface

The form drag $\tau^w_{s\alpha}$ and the wave energy flux at the sea surface F^w_s are the governing parameters of the mod-

el. Unfortunately, the experimental estimates of these fluxes for the ocean swell are lacking. However, useful information related to this study can be extracted from a laboratory experiment by Donelan (1999) who directly measured the growth and attenuation rates of waves propagating along and opposite to the wind. Waves propagating along the wind were generated by this wind. In order to generate waves propagating against the wind, a wavemaker (paddle) was used. Donelan found that the growth/attenuation rate of the wave energy E could be parameterized by

$$\beta = \frac{1}{\Omega E}\frac{\partial E}{\partial t} = c_\beta \frac{\rho_a}{\rho_w}\left(\frac{\overline{u}_{\lambda/2}}{C} - 1\right)\left|\frac{\overline{u}_{\lambda/2}}{C} - 1\right|, \quad (25)$$

where $\overline{u}_{\lambda/2}$ is the wind velocity at height $x_3 = \pi/K$ and c_β is an empirical constant, which is equal to 0.28 for waves traveling along the wind and 0.11 for waves traveling opposite the wind. Measurements were performed in the range of the dimensionless inverse wave age parameter $|\overline{u}_{\lambda/2}/C|$ from 3 to 7 for the wind-generated waves propagating along the wind, and from 1.5 to 4.5 for the paddle-generated waves propagating against the wind. The question arises, however, whether the parameterization (25) could be used for the ocean swell, which is characterized by much smaller values of the inverse wave age parameter. Taking for the ocean swell the typical value of the phase velocity $C = 15$ m s^{-1} and the wind speed $\overline{u}_{\lambda/2} = 3$ m s^{-1} results, according to (25), in $\beta = -2 \times 10^{-4}$ for opposite-wind swell and $\beta = -0.9 \times 10^{-4}$ for following-wind swell, which means that the spatial scale of swell attenuation $L = (\beta\Omega)^{-1}C_g$ (C_g is the swell group velocity) is $L \simeq 50$ km and $L \simeq 130$ km, respectively. This estimate shows that the parameterization (25) being applied to the ocean swell (extrapolated to lower values of the inverse wave age parameter) gives too large of an attenuation rate. It is a known fact that swell may propagate large distances (thousands of kilometers) across the ocean (e.g., Snodgrass et al. 1966). It is concluded that the parameterization (25) cannot be directly applied to the ocean swell. It is valid only in the range of measurements. The latter fact will be used further in the derivation of the analytical expression of swell attenuation.

Expressions describing the growth/attenuation rate of a surface wave traveling at an arbitrary angle with respect to the wind direction are based on the simplified model of the airflow above waves by Kudryavtsev et al. (2001), and its extension to account for the arbitrary wind direction by Meirink et al. (2003). The details of the derivation are given in the appendix. The attenuation/growth rate of the wave due to the work of the surface stress against the wave orbital velocity described by the second term on the right-hand side of (8) is given by (A24). Correspondingly the energy flux at the sea surface due to the work of the shear stress is expressed through β_τ as

$$F^w_{s\tau} \equiv \overline{\tilde{u}_s\tilde{\tau}_{s1}} = \frac{1}{2}\beta_\tau C^3(AK)^2. \quad (26)$$

The energy flux due to the action of pressure correlated with the wave slope is described by the first term on the right-hand side of (8). The parameterization of the growth rate parameter β_p is given by (A29) in the appendix. In terms of β_p the energy flux at the sea surface due to the action of pressure is

$$F^w_{\rm sp} = C\overline{\tilde{p}_s z_1} = \frac{1}{2}\beta_p C^3(AK)^2. \quad (27)$$

The total energy flux is

$$F^w_s \equiv F^w_{s\tau} + F^w_{\rm sp} = \frac{1}{2}(\beta_\tau + \beta_p)C^3(AK)^2. \quad (28)$$

Correspondingly, the form drag supported by swell [(4)] is

$$\tau^w_{s1} = \overline{\tilde{p}_s z_1} = \frac{1}{2}\beta_p C^2(AK)^2. \quad (29)$$

Figures 2 and 3 show the growth rate parameters β_p and β_τ obtained according to (A24) and (A29), and by numerical calculations based on the model of Meirink et al. (2003). Results are presented in terms of the growth rate coefficient defined as

$$C^\beta_{[\tau,p]} = \beta_{[\tau,p]}\frac{\rho_w}{\rho_a}\left(\frac{C}{u_*}\right)^2. \quad (30)$$

In calculations a wave with an infinitesimal slope was assumed, so that its influence on the mean structure of the MABL is negligible. In this case the friction velocities in the IR and in the OR are equal (i.e., $\upsilon_* = u_*$), and the TKE b inside the IR is $b = u_*^2$. Figure 2 displays $C^\beta_{[\tau,p]}$ and their sum $C^\beta = C^\beta_p + C^\beta_\tau$ as a function of the angle θ between the wind and the wave direction for three values of the inverse wave age parameter defined in the 0° angle direction; namely, $|\overline{u}_\lambda|/C = 0.3$, 1.5, and 8. Swell is traditionally defined as waves that do not receive energy from the wind. For waves traveling along the wind direction that are propagating faster than the wind; that is, $\overline{u}_\lambda \cos\theta/C < \sim 1.2$. At opposite- and cross-wind directions all waves can be regarded as swell, as they attenuate on the wind. In oceans, when the wind rapidly turns, the value of $|\overline{u}_\lambda|/C$ can be rather high ($\sim$1.5). Case $|\overline{u}_\lambda|/C = 8$ represents a pure wind-sea case when waves actively receive energy from the wind at the following- and close to following-wind directions. At the opposite-wind direction this case represents swell generated in laboratory conditions (Donelan 1999). For the pure swell case, $|\overline{u}_\lambda|/C = 0.3$, both mechanisms (work of the stress and pressure) are equally important in the transfer of energy from swell to the wind. The angular distribution is very asymmetric: moving from 0° to 90° the absolute magnitude of the attenuation rate decreases. Moving farther to 180° it rapidly increases. The rate of attenuation is 2 times

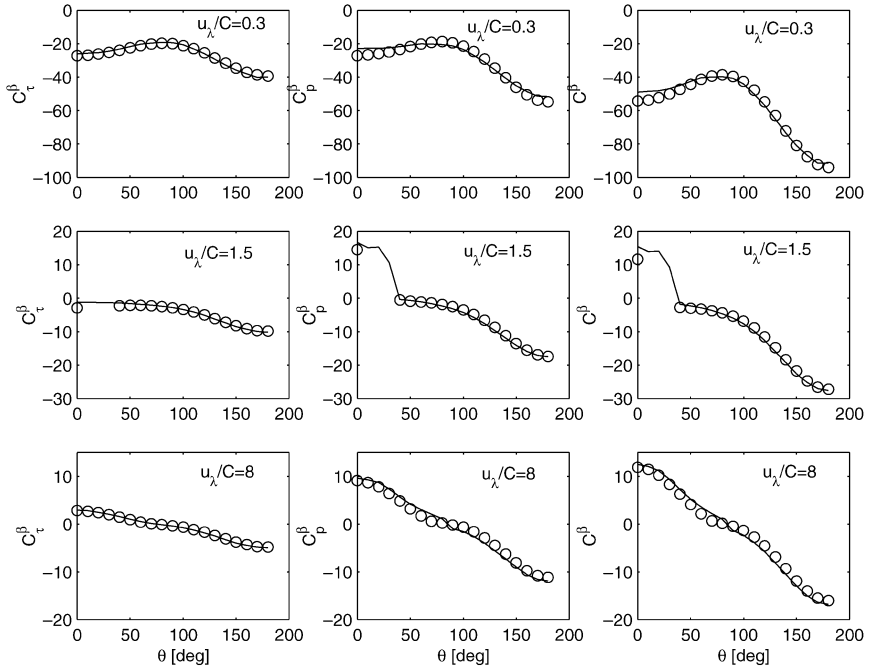

FIG. 2. Growth rate coefficient defined by (30) as a function of the swell-wind angle: (left) C^{β}_{τ}, (middle) C^{β}_{p}, and (right) their sum $C^{\beta} = C^{\beta}_{\tau} + C^{\beta}_{p}$. The inverse wave age parameter $|u_{\lambda}|/C$ = (top) 0.3, (middle) = 1.5, and (bottom) = 8. Solid lines are (A24) and (A29) and their sum; circles are model results of Mierink et al. (2003).

as large for the opposite-wind direction than for the following-wind direction. Case $|\overline{u}_{\lambda}|/C = 1.5$ represents a ''mixed wind sea–swell sea.'' The pressure term is dominant in the following-wind direction, but with an increase of the angle it rapidly falls to zero and becomes negative. In the cross- and opposite-wind directions both terms are important in swell attenuation. At high values of $|\overline{u}_{\lambda}|/C$ the pressure mechanism dominates and provides the growth of surface waves propagating at an angle $-90° < \theta < 90°$ to the wind. At an angle $90° < \theta < -90°$ they attenuate. Notice that at large $|\overline{u}_{\lambda}|/C$ the angular distribution of C^{β} is very close to $\cos\theta|\cos\theta|$, as was mentioned by Meirink et al. (2003).

The distribution of $C^{\beta}_{[\tau,p]}$ and their sum C^{β} as a function of the inverse wave age parameter $|\overline{u}_{\lambda}|/C$ for the following-wind swell ($\theta = 0°$), cross-wind swell ($\theta = 90°$), and opposite-wind swell ($\theta = 180°$) is shown in Fig. 3. The pressure term dominates the stress term for the wind-sea waves. For swell $\overline{u}_{\lambda}/C < \sim 1.2$ the terms are equal. For cross- and opposite-wind swells both mechanisms are equally important. The magnitude of the attenuation rate is maximal for the opposite-wind swell. In the whole range of the inverse wave age parameter and the angle, the expressions obtained approximate the model results of Meirink et al. (2003) with reasonable accuracy.

By comparing obtained values of C_{β} with measurements (e.g., Plant 1982; Donelan 1999) it becomes clear that they are several times as small as the measured values in the range of data validity, that is, for slowly propagating waves $|\overline{u}_{\lambda}|/C > 2$. This is a known feature of the wind-over-waves theoretical models based on the Reynolds equations (e.g., Townsend 1972; Belcher and Hunt 1993; Mastenbroek et al. 1996). Recently Kudryavtsev and Makin (2002) showed that this discrepancy can be partly explained by the variation along the wave profile of the aerodynamic surface roughness (mainly due to modulation of small-scale breaking waves), which leads to an increase of the modeled wave growth/attenuation rate. An accurate account of this effect is out of the scope of the present study.

To assess the impact of swell on the sea drag, the right magnitude of the swell attenuation rate is needed. It is assumed that (A24) and (A29) correctly reproduce the spectral and angular behavior of β_{τ} and β_{p} in the whole range of wind and wave parameters considered. Then a proportionality factor f_{β} is introduced, which allows for fitting the magnitude of the modeled growth rate $\beta = \beta_{r} + \beta_{p}$ to the measured values in the range of data validity, that is, at $|\overline{u}_{\lambda/2}|/C > 2$. The growth rate according to parameterization (25) and the modeled value $f_{\beta}\beta$ with $f_{\beta} = 5$ are shown in Fig. 4. Corrected in this way, the modeled growth rate is now consistent with measurements for both following- and opposite-wind waves. Last, it is assumed that expressions (A24) and (A29) multiplied by 5 are also valid in the range of $|\overline{u}_{\lambda/2}|/C$ not covered by measurements, that is, at $|\overline{u}_{\lambda/2}|/C < 2$. These corrected expressions (their sum) are used further in the study. Considering again the ocean swell with $C = 15$ m s^{-1} and $\overline{u}_{\lambda/2} = 3$ m s^{-1} the

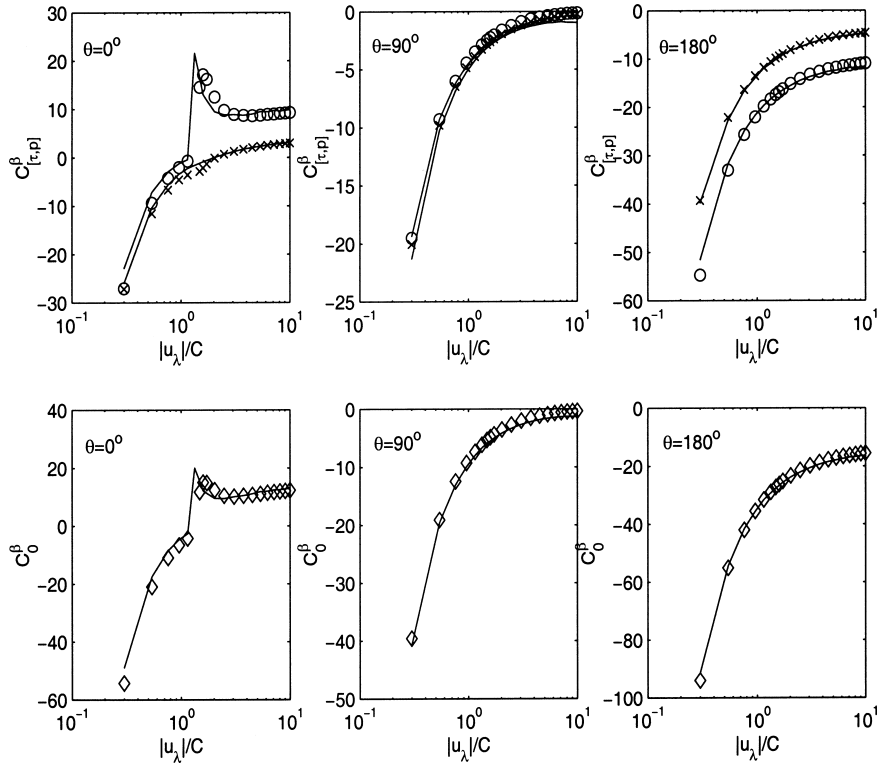

FIG. 3. Growth rate coefficient defined by (30) as a function of the inverse wave age parameter $|u_\lambda|/C$: (top) $C^{\beta}{}_{[\tau,p]}$ and (bottom) their sum $C^{\beta} = C^{\beta}_{\tau} + C^{\beta}_{p}$. Results are shown for different swell-wind angles: (left) $\theta = 0°$, (middle) $\theta = 90°$, and (right) $\theta = 180°$. Solid lines are (A24) and (A29) and their sum; open circles are modeled C^{β}_{p}; crosses are modeled C^{β}_{τ}; triangles are modeled C^{β}.

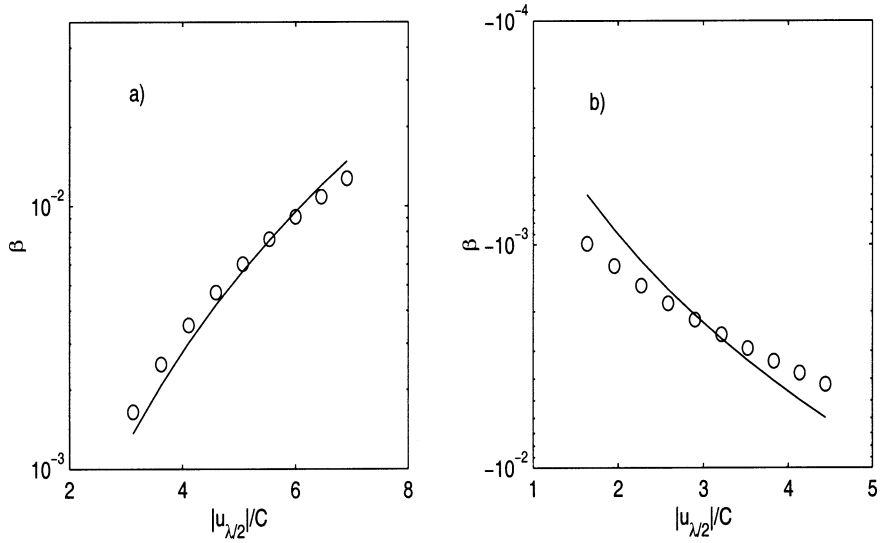

FIG. 4. (a) Growth rate for the wind waves. (b) Attenuation rate for the paddle-generated waves traveling opposite the wind. Open circles are parameterization (25) of Donelan (1999); solid lines are defined as the sum of (A24) and (A29) multiplied by a factor of 5. Range of the inverse wave age parameter $|u_{\lambda/2}|/C$ corresponds to measurements by Donelan (1999).

corrected values of the attenuation rate are $\beta = -1.8 \times 10^{-5}$ for opposite-wind swell and $\beta = -1.2 \times 10^{-5}$ for following-wind swell. Corresponding spatial scales of swell attenuation are $L \simeq 600$ and 1000 km. This scale is 10 times that predicted by (25).

3. Model results

In this section the impact of ocean swell on the sea drag is studied using the model developed above. The equations describing the impact of swell on the MABL are the resistance law (23), the TKE balance equation (21), the momentum balance equation (2), and equations for the wave-induced momentum flux (29), the wave energy flux at the sea surface (28), the scale of the IR, and for the wind velocity profile in the IR (20) and OR (22). The input parameters to the model are the wind speed and the angle between the wind and swell propagation direction, the phase velocity, and the slope of the swell. Equations are solved by iterations starting from a no-swell MABL state and resulting in a new MABL state adjusted to the presence of swell. As the swell attenuation rate β_τ (A24) and β_p (A29) and, consequently, the wave-induced momentum flux τ_s^w and the wave energy flux F_s^w are functions of local parameters of the MABL, namely, the friction velocity in the IR, swell and the MABL form a coupled system with a feedback between the swell and the atmosphere.

We are interested in the ocean swell characterized by a small value of the inverse wave age parameter $|\overline{u}_\lambda|/C < 1.2$ when the pronounced impact of swell on the boundary layer is expected. The characteristic slope of swell in the ocean is $AK < 0.1$ and the phase velocity is $10 < C < 30$ m s^{-1}. Results are presented in terms of the drag coefficient at 10-m height,

$$\mathrm{CD}_{10} = \left(\frac{u_*}{u_{10}}\right)^2, \tag{31}$$

and the drag coefficient at the sea surface defined as

$$\mathrm{CD}_{\mathrm{sur}} = \left(\frac{\upsilon_*}{u_{10}}\right)^2, \tag{32}$$

where u_{10} is the wind speed at 10-m height. In real conditions the reference level of 10 m is always located in the OR so that u_* is the friction velocity in the outer region, while υ_* is the surface friction velocity located inside the IR. The surface friction velocity is an important parameter for a number of applications (e.g., generation of capillary–gravity waves, and for gas, heat, and moisture transfers, etc.), as all of these processes are governed by the turbulent momentum flux at the sea surface. When the impact of swell is pronounced and the form drag is comparable to the turbulent stress, the surface friction velocity defined through the surface turbulent stress differs from the friction velocity taken far away from the surface.

Figure 5 displays CD_{10} as a function of the wind speed

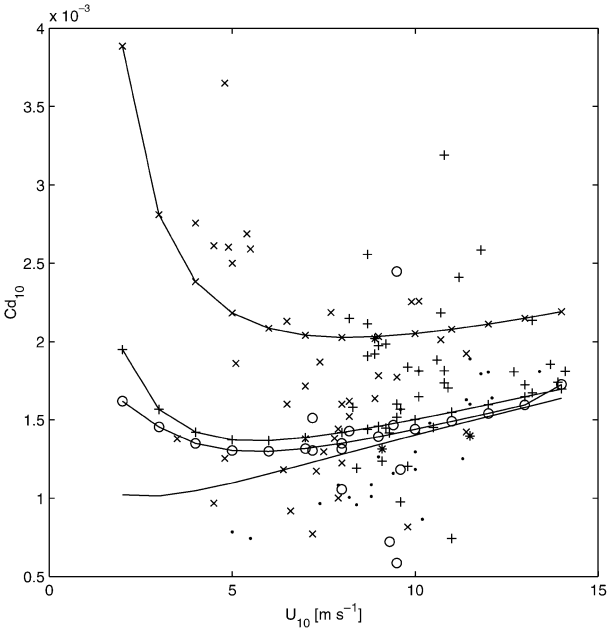

FIG. 5. Modeled and measured drag coefficient CD_{10} at 10-m height as a function of the wind speed u_{10} and for different swell-wind angles: following-wind swell (solid line with open circles: modeled $\theta = 0°$; open circles: data), cross-wind swell (solid line with pluses: modeled $\theta = 90°$; pluses: data), and opposite-wind swell (solid line with crosses: modeled $\theta = 180°$; crosses: data). No-swell case (solid line: modeled; dots: data). The swell slope $AK = 0.06$, and the phase velocity $C = 15$ m s^{-1}, swell parameters typical for the ocean experiments of Donelan et al. (1997) and Drennan et al. (1999). Data are taken from Donelan et al. (1997, their Table 1).

for following-, cross-, and opposite-wind swell. The swell slope and the phase velocity are specified in the model as $AK = 0.06$ and $C = 15$ m s^{-1}, values that are typical for the experiment in the open ocean presented in Donelan et al. (1997). The experimental data of Donelan et al. (1997) (taken from their Table 1) are also shown in Fig. 5. According to the model, the impact of swell is quite pronounced for a low wind speed, $u_{10} < 6$ m s^{-1}. It increases with as the angle between the swell and the wind increases, and is maximum for opposite-wind swell. These features are consistent with Donelan et al.'s (1997) data. The model magnitude of the drag coefficient at low winds and opposite-wind swell in general agrees with experimental estimates by Donelan et al. (1997) though the scatter in the data is large. This qualitative and quantitative agreement with observations is encouraging, and below the impact of swell on the MABL is analyzed in more details.

In Fig. 6 the drag coefficient CD_{10} and the surface drag coefficient $\mathrm{CD}_{\mathrm{sur}}$ for following-, cross-, and opposite-wind swell characterized by the phase velocity $C = 15$ m s^{-1} and the slope $AK = 0$ (no swell), $AK = 0.05$, and $AK = 0.1$ are shown as a function of the wind speed. The obvious result is that the impact of swell drastically depends on the swell slope AK, increasing as the slope is increased. This directly follows from (26),

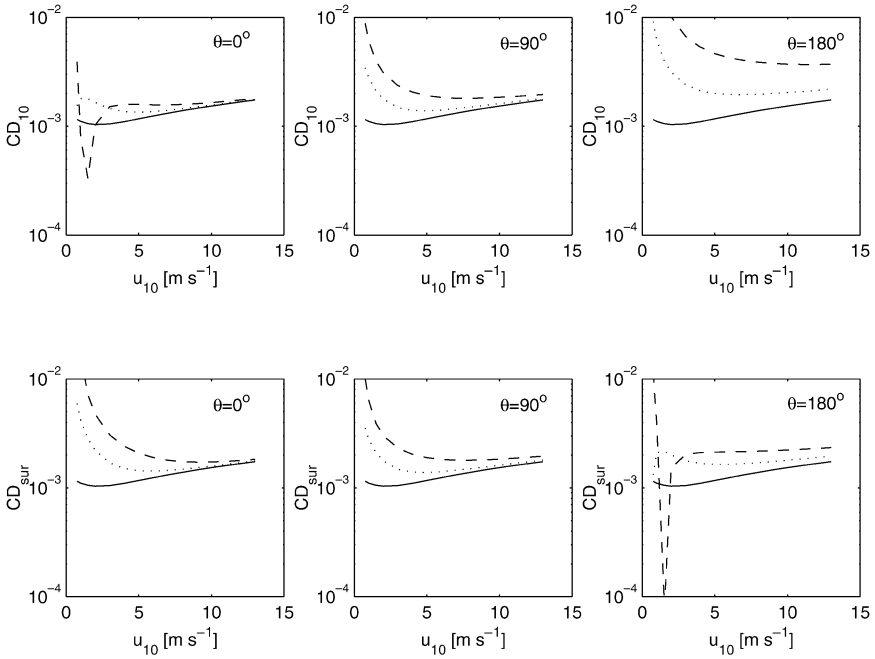

FIG. 6. (top) Modeled drag coefficient CD_{10} at 10-m height, and (bottom) the surface drag coefficient CD_{sur} as a function of the wind speed u_{10} and for different swell-wind angles. (left) Following-wind swell $\theta = 0°$, (middle) cross-wind swell $\theta = 90°$, and (right) opposite-wind swell $\theta = 180°$. No-swell case is solid lines; the swell slope $AK = 0.05$ is dotted lines; the swell slope $AK = 0.1$ is dashed lines. The swell phase velocity is $C = 15$ m s^{-1}.

(27), and (29) because energy and momentum transfers are proportional to the slope squared. Another anticipated result is that the impact is most pronounced at low winds as the parameter u_{10}/C (or u_*/C) goes down and the wave-induced fluxes dominate the turbulent fluxes. As was already mentioned above, the impact of swell on CD_{10} is strongest in the opposite-wind direction.

For following-wind swell the magnitude of the surface turbulent stress (surface drag coefficient CD_{sur}) at low winds considerably exceeds the stress in the no-swell case and is larger than CD_{10}. As swell attenuates and transforms energy and momentum to the atmosphere the surface turbulent stress inside the IR should be increased compared to the no-swell case. This directly follows from the condition of the constant-flux layer (2): as $\tau_1^w(0) < 0$, the surface turbulent stress $\overline{\tau}_1(0)$ should be increased to compensate for the negative wave-induced flux and keep τ_0 constant with height. In fact their sum τ_0 appears to be slightly larger than the initial turbulent flux in the no-swell case. This leads to a slight increase of the turbulent stress in the OR and thus CD_{10} as compared to the no-swell case. For cross- and especially for opposite-wind swell the situation is quite different. For cross-wind swell, CD_{sur} and CD_{10} are comparable. This is due to the generation of the stress component being aligned with the direction of swell propagation. For opposite-wind swell CD_{sur} is only slightly larger than in the no-swell case while CD_{10} is increased considerably. This is explained by the following. The surface turbulent stress is increased as compared to the no-swell case because swell generates additional turbulence in the IR. The momentum is transferred from swell to the wind so that $\tau_1^w(0) < 0$. The surface turbulent stress is also negative, $\overline{\tau}_1(0) < 0$, as the wind is in the opposite direction. Both stresses combine to increase considerably the absolute value of the total stress τ_0 and thus the turbulent stress in the OR and the CD_{10}.

There are two peculiarities observed: one is the minimum of CD_{10} for the following-wind steep swell, and the other is the minimum of CD_{sur} for the opposite-wind steep swell, both at a very low wind. To find out the cause of these peculiarities let us consider the dependence of the TKE inside the IR and the wind velocity profile in the MABL on the wind and swell parameters. Swell transfers its energy to the atmosphere, providing the additional source of the TKE. According to (21) it enhances the TKE inside the IR as compared with the no-swell case. In the no-swell case the TKE $b = v_*^2 = u_*^2$, so that in the presence of swell b is always larger than v_*^2. That is illustrated in Fig. 7, where b/u_{10}^2 is plotted as a function of the wind speed and the slope (cf. with values of $CD_{sur} = v_*^2/u_{10}^2$ plotted in Fig. 6).

The wind profile is shown in Fig. 8. As swell loses momentum to the atmosphere ($\tau_1^w < 0$), the wind velocity gradient

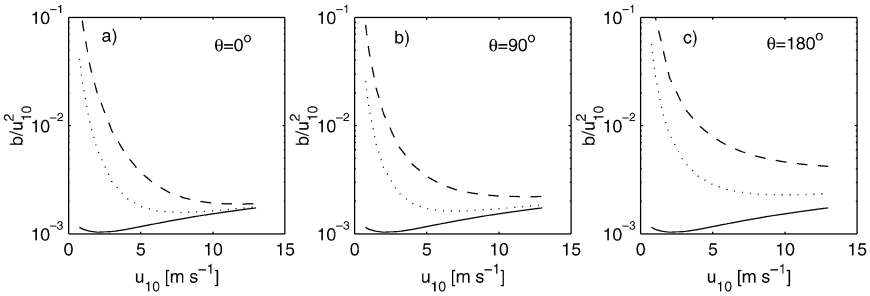

FIG. 7. Turbulent kinetic energy b/u_{10}^2 in the IR [(21)] as a function of the wind speed u_{10} and for different swell-wind angles: (a) following-wind swell $\theta = 0°$, (b) cross-wind swell $\theta = 90°$, and (c) opposite-wind swell $\theta = 180°$. No-swell case is solid lines; the swell slope $AK = 0.05$ is dotted lines; the swell slope $AK = 0.1$ is dashed lines. The swell phase velocity is $C = 15$ m s^{-1}.

$$\frac{d\overline{u}_\alpha}{d\ln\varsigma} = \frac{\tau_{0\alpha} - \tau_\alpha^w}{\kappa b^{1/2}}$$

deviates from one in a no-swell case. In the following-wind direction and a very low wind speed the airflow inside the IR is accelerated in comparison with a no-swell case. This effect generates a swell-driven wind, which is quite pronounced in Fig. 8a in the form of the jetlike shape of the wind profile. The maximum of the wind velocity is located at the IR height. In this case the shear stress below the IR height is positive, while that above is negative (the momentum flux is directed upward). With an increase of the wind speed the bump in the wind profile disappears, and the shear stress in the OR also becomes positive. A change of the sign of the shear stress in the OR explains the origin of the minimum of CD_{10} in Fig. 6.

Figure 8b illustrates the wind velocity profile for opposite-wind swell. As the x_1 axis is directed along the swell direction the wind velocity at the reference level is negative. In this case swell transfers the momentum to the IR and decelerates the airflow reducing the absolute wind speed. At a very low wind this effect could causes a reverse flow. A change of the sign of the shear stress in the IR explains the existence of the CD_{sur} minimum in Fig. 6. At all wind speeds the airflow in the IR is decelerated as compared with the no-swell condition, which results in the enhanced drag coefficient at the reference level CD_{10} (see also explanation above in terms of the stress).

Cross-wind swell (Figs. 8c,d) loses its momentum and generates the x_1 component of the wind velocity (Fig. 8c). This leads to the rotation of the wind vector with height. In this way cross-wind swell causes the difference between the wind and the shear stress vectors. This effect is illustrated in Fig. 9 for the turbulent stress in the OR and in the IR. As before, the effect is proportional to the swell slope and weakens as the wind speed increases. In general the deviation of the shear stress in the OR and in the IR has the opposite sign with respect to the wind direction at the reference level. When the angle between the wind direction and the swell is $0° < \theta < 180°$, the shear stress in the OR deviates to the left from the wind vector, while the surface stress deviates to the right. The situation is opposite when $180° < \theta < 360°$.

Generation of wave-driven wind was observed by Harris (1966) in a wave tank experiment. Harris revealed that the paddle wave generates the mean air motion in the initially still air above. His measurements of the wind velocity caused by the paddle wave with period 0.82 s and amplitude 5.1 cm (wave height 10.2 cm) at three fixed levels are shown in Fig. 10. The experiment evidently shows the existence of wave-driven wind. Though the measurements are on three levels only, one can see that the wave-driven wind speed increases toward the water surface. The model simulation was performed for the same wave parameters and given 0 ambient wind speed at the reference level of 6 m [that is equal to the roof height in the experiment by Harris (1966)]. The model simulation shown in Fig. 10 exhibits a jetlike wind velocity profile with a maximum at the IR height. Above the IR the wind speed decreases with height as was observed in the experiment. The maximum of the wind speed profile is not resolved by the measurements, as they were done in the fixed coordinate system above the wave crest (i.e., above the IR height). The model simulation is performed in the wave-following coordinate system. However, above the wave crest at the level of measurements the wind speeds in the wave-following and fixed coordinate systems are not distinguishable. The model reproduces the effects of generation of wave-driven wind in the laboratory conditions, though the observed wind speed is somewhat higher than the modeled.

The dependence of CD_{10} and CD_{sur} on the swell phase velocity in the range of $10 < C < 30$ m s^{-1} for following-, cross-, and opposite-wind swell with the slope $AK = 0.05$ is shown in Fig. 11. When the phase velocity increases, the impact of swell becomes more and more pronounced. This follows directly from (28) and (29), describing the wave-induced energy and momentum flux. Being normalized on the wind speed (or the friction

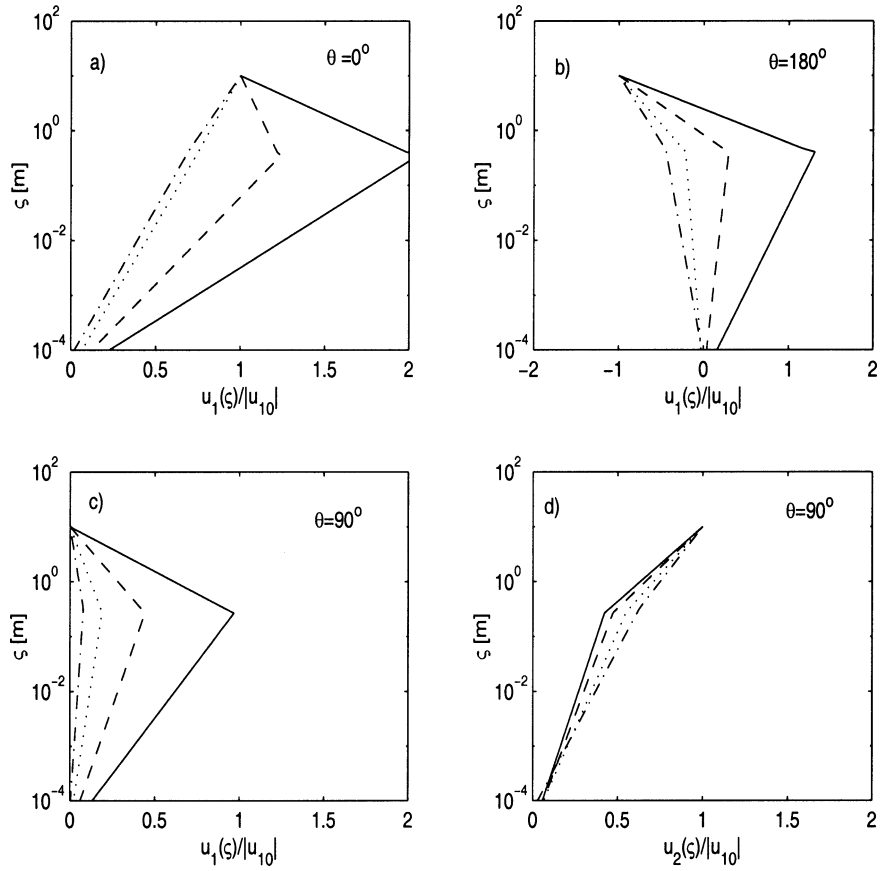

FIG. 8. Vertical profile of the wind velocity normalized on the wind speed u_{10} in the presence of swell with the slope $AK = 0.1$ and phase velocity $C = 15$ m s^{-1}: (a) following-wind swell; (b) opposite-wind swell; (c) cross-wind swell, x_1 component (along the swell direction) of the wind velocity; and (d) cross-wind swell, x_2 component (across the swell direction) of the wind velocity. Solid lines: $u_{10} = 0.5$ m s^{-1}; dashed: $u_{10} = 1.0$ m s^{-1}; dotted: $u_{10} = 2.0$ m s^{-1}; dashed–dotted: $u_{10} = 4.0$ m s^{-1}.

velocity), the dimensionless fluxes are proportional to the wave age parameter C/u_{10} (or C/u_*). Decreasing u_{10}, fixing C, or increasing C with the wind speed fixed leads to the increase of the wave-induced fluxes and thus the swell impact on the drag.

4. Conclusions

Swell propagating over the ocean interacts with the atmosphere and loses its momentum and energy to the wind. The exchange of energy is realized through two mechanisms: through the correlation of the surface pressure with the rate of change of the wave surface (vertical orbital velocity), and through the work of the surface turbulent stress against the wave orbital velocity. For ocean swell characterized by a small absolute value of the inverse wave age parameter $|u_{10}\cos(\theta)/C| < 1.2$, both mechanisms are equally important. The attenuation rate is maximal for opposite-wind swell, and in this case swell attenuates 2 times as fast as the following-wind swell.

A model that accounts for the impact of swell on the marine atmospheric boundary layer is described. The model is based on the two-layer approximation of the MABL: the near-surface inner region and the outer region above. The wave-induced momentum and energy fluxes are confined within the IR, so that the IR is directly affected by swell. Swell transfers energy to the atmosphere and enhances the turbulent kinetic energy in the IR. The transfer of momentum results in acceleration or deceleration of the airflow near the surface, which leads to the fact that the surface turbulent stress differs from the turbulent stress (sea drag) far above the sea surface. Following-wind swell accelerates the flow, which for a very low wind results in the jetlike profile of the wind velocity (swell-driven wind) with its maximum at the IR height. In this case the surface stress is strongly enhanced, while the sea drag is less affected. Opposite-wind swell decelerates the airflow, which for a steep swell could cause the reverse airflow. The sea drag in this case is considerably enhanced as compared with the following-wind swell case. Cross-wind swell

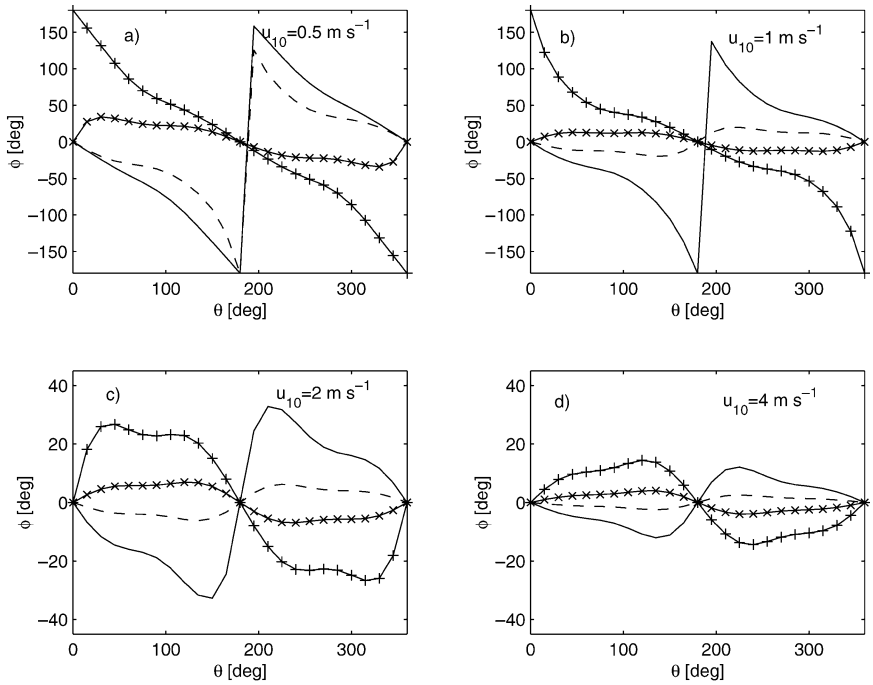

FIG. 9. Angle between the turbulent shear stress vector and the wind velocity at 10-m-height vector as a function of the swell-wind angle θ: (a) $u_{10} = 0.5$, (b) $u_{10} = 1.0$, (c) $u_{10} = 2.0$, and (d) $u_{10} = 4.0$ m s^{-1}. The swell phase velocity $C = 15$ m s^{-1}. Solid lines with pluses and crosses show the turbulent stress at 10-m height and the swell slopes $AK = 0.1$ and $AK = 0.05$, respectively. Solid lines and dashed lines show the turbulent stress at the surface and the swell slopes $AK = 0.1$ and $AK = 0.05$, respectively.

causes the rotation of the wind velocity vector with height, which leads to the deviation of the turbulent stress vector from the wind velocity vector. All of these peculiarities in the wind profile and the stress are quite pronounced at very low winds and disappear as the wind speed increases or as the swell phase velocity decreases. In fact, it is the inverse wave age parameter $|u_{10}|/C$ (or u_*/C) that characterizes the impact: the smaller $|u_{10}|/C$, the stronger is the impact of the swell on the MABL. The impact of swell directly depends on the swell slope being more pronounced for a steeper swell. This is because both the wave-induced momentum and the energy fluxes increase rapidly with an increase of the slope.

Given the values of the wind speed, the swell phase velocity, and the slope typical for the ocean experiments of Donelan et al. (1997) and Drennan et al. (1999), the model is able to reproduce qualitatively and quantitatively the main experimental findings: the impact of swell on the sea drag is well pronounced for opposite-wind swell, less pronounced for cross-wind swell, and occurs only at low wind speeds $u_{10} < 6$ m s^{-1}. At low winds (and zero ambient wind) the model predicts the existence of well-pronounced wave-driven wind, observed, for example, by Harris (1966) in the laboratory. We remind the reader that the model possesses a tuning constant $f_\beta = 5$, which was chosen to fit the model wind attenuation/growth rate to the laboratory data of Donelan (1999). Since only these laboratory data are currently available (at least for the attenuation rate), future corrections of the magnitude of the attenuation rate of swell in real conditions could result in the revision of the effects of swell on the atmospheric boundary layer.

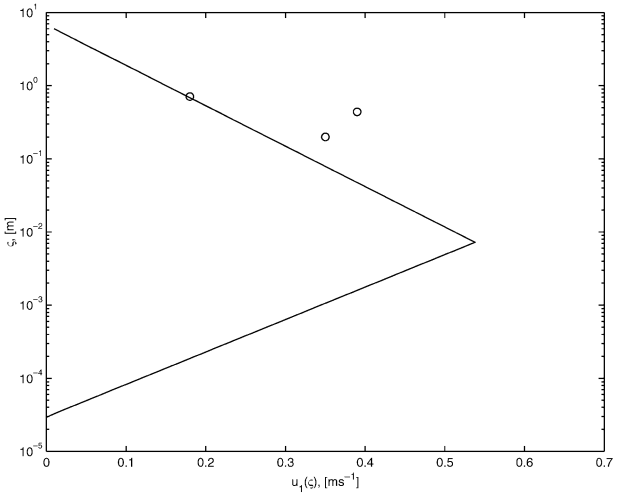

FIG. 10. Vertical distribution of wave-driven wind: solid line is modeled; open circles are data from Harris (1966).

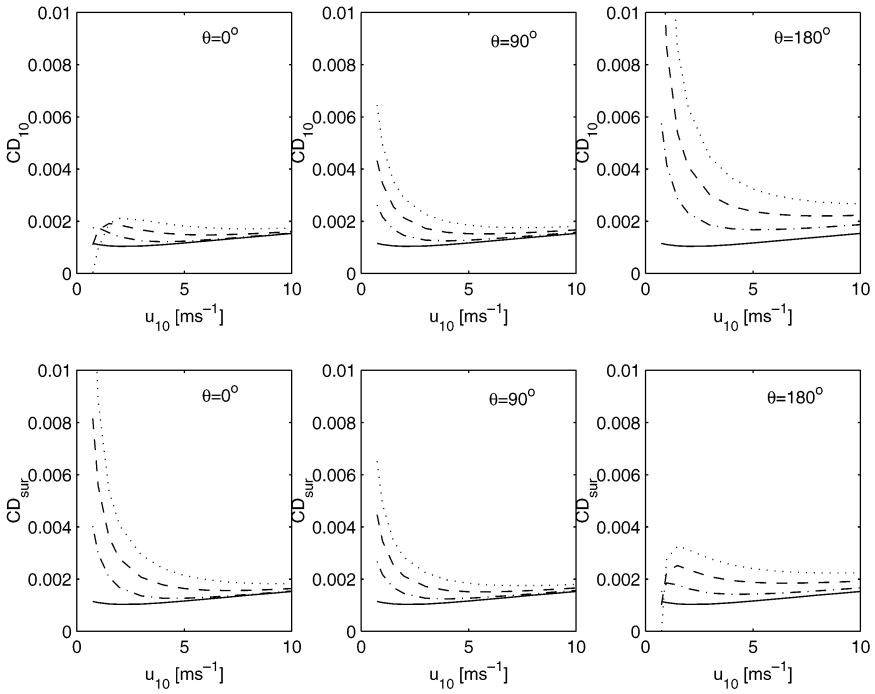

FIG. 11. (top) Drag coefficient CD_{10} at 10-m height and (bottom) the surface drag coefficient CD_{sur} as a function of the wind speed u_{10} and for different swell-wind angles: (left) following-wind swell $\theta = 0°$, (middle) cross-wind swell $\theta = 90°$, and (right) opposite-wind swell $\theta = 180°$. No-swell case is solid lines; the swell phase velocity $C = 10$ m s^{-1} is dashed–dotted lines; $C = 20$ m s^{-1} is dashed lines; $C = 30$ m s^{-1} is dotted lines. The swell slope is $AK = 0.05$.

Acknowledgments. The authors acknowledge the support by the Netherlands Organization for Scientific Research (NWO) through the Dutch–Russian Scientific Co-operation Programme 2001, Project 047.014.009, and by the Office of Naval Research (ONR), Grant N00014-03-1-0619 (PR No. 03PR09880-00). VNK acknowledges the support of the Norwegian Space Centre under Contract JOP.8.3.3.06.01.2., and INTAS cooperation via Project INTAS-01-234.

APPENDIX

Interaction of Turbulent Airflow with a Surface Wave

a. Governing equations

A wave-following orthogonal coordinate system (ξ_1, ξ_2, ξ_3) defined as

$$\xi_1 = x_1 + Ae^{-Kx_3}\sin Kx_1, \tag{A1}$$

$$\xi_2 = x_2, \quad \text{and} \tag{A2}$$

$$\xi_3 = x_3 - Ae^{-Kx_3}\cos Kx_1 \tag{A3}$$

is used in the present study (e.g., Sullivan et al. 2000). As it follows from (A3), the surface $\xi_3 = 0$ coincides with the wavy surface (1): $z = A\cos Kx_1$. The Navier–Stokes equations

$$\frac{\partial u_i}{\partial t} + \frac{\partial}{\partial x_j}(u_i u_j) = -\frac{\partial p}{\partial x_i} - f_i \tag{A4}$$

and the continuity equation

$$\frac{\partial u_j}{\partial x_j} = 0 \tag{A5}$$

written above in the Cartesian coordinate system, in the wave-following ξ-coordinate system, take the form

$$\frac{1}{J}\frac{\partial u_i}{\partial t} + \frac{\partial}{\partial \xi_j}(u_i \upsilon_j) = -\frac{\partial}{\partial \xi_j}\left(\frac{\xi_{j,i}p}{J}\right) - f_i \quad \text{and} \tag{A6}$$

$$\frac{\partial \upsilon_j}{\partial \xi_j} = 0, \tag{A7}$$

where u_i is the wind velocity component in the Cartesian coordinate system x_i, p is the pressure normalized on the air density, f_i is the component of the molecular viscosity force, $\xi_{j,i} = \partial\xi_j/\partial x_i$, $J = \xi_{1,1}\xi_{3,3} - \xi_{1,3}\xi_{3,1}$ is the Jacobian of the coordinate system transformation, and υ_i is the component of the contravariant flux velocity defined by

$$\upsilon_i = u_j\xi_{i,j}/J. \tag{A8}$$

To derive (A6) and (A7), the identity

$$\frac{\partial}{\partial \xi_j}\left(\frac{\xi_{j,i}}{J}\right) = 0 \tag{A9}$$

was used.

b. Momentum and energy conservation equations

Any airflow quantity y can be split into a sum of the mean (averaged over ξ_1 and ξ_2 : $\overline{y}$), the wave-correlated (defined as a deviation of y averaged over ξ_2 at given ξ_1 $\langle y\rangle$ from its mean value $\overline{y}:\tilde{y} = \langle y\rangle - \overline{y}$), and the random (turbulent) ($y' = y - \langle y\rangle$) components. For example, the decomposition of the air pressure is

$$p = \overline{p} + \tilde{p} + p'. \tag{A10}$$

Averaging of (A6) over ξ_2 at a given ξ_1 results in the following equation:

$$\frac{1}{J}\frac{\partial\langle u_i\rangle}{\partial t} + \frac{\partial}{\partial \xi_j}(\langle u_i\rangle\langle v_j\rangle) = -\frac{\partial}{\partial \xi_j}(\xi_{j,i}J^{-1}\langle p\rangle) + \frac{\partial}{\partial \xi_j}(\tau_{ij}), \tag{A11}$$

where the action of the molecular viscosity force on the mean and the wave-induced motion is neglected; $\tau_{ij} = -\langle u_i' v_j'\rangle$ is the tensor of the turbulent stress based on the multiplication of the Cartesian and contravariant velocity components. The one-dimensional momentum conservation equation for the horizontal component is found by averaging (A11) over ξ_1 and reads

$$\frac{\partial}{\partial \xi_3}(\tau_\alpha^w + \tau_\alpha) = 0, \tag{A12}$$

where $\alpha = 1$ or 2, $\tau_\alpha = \overline{\tau}_{\alpha 3}$ is the component of the turbulent shear stress, and τ_α^w is the wave-induced momentum flux defined as

$$\tau_\alpha^w = -\overline{\tilde{u}_\alpha \tilde{v}_3} - \overline{\tilde{p}\xi_{3,\alpha}/J}. \tag{A13}$$

Equation (A12) provides the condition of the constant-flux layer: the sum of the wave-induced stress and the shear stress $\tau_\alpha^w + \overline{\tau}_\alpha$ is constant over the height and is equal to the vertical flux of the horizontal momentum $\tau_{0\alpha}$ far away from the sea surface; that is,

$$\tau_\alpha^w + \tau_\alpha = \tau_{0\alpha}. \tag{A14}$$

The conservation equation for the wave-induced energy can be derived by multiplying (A11) by $\langle u_i\rangle$ and averaging the obtained equation over the horizontal space

$$\frac{\partial}{\partial \xi_3}F^w + \tau_\alpha^w\frac{\partial U_\alpha}{\partial \xi_3} - \overline{\tilde{\tau}_{ij}\frac{\partial \tilde{u}_i}{\partial \xi_j}} = 0, \tag{A15}$$

where F^w is the energy flux of the wave motion:

$$F^w = -\overline{\tilde{p}\tilde{u}_3} + \overline{\tilde{u}_j\tilde{\tau}_{j3}}, \tag{A16}$$

and $U_\alpha = \overline{u}_\alpha - C$. The expression for F^w is written with second-order accuracy in the wave slope. To derive (A15), (A12) is used, which, being multiplied by U_α, gives the energy conservation equation for the mean flow (its explicit form is not needed here). Equation (A15) shows that the energy of the wave-induced motion is provided by the balance of the divergence of the wave energy flux, the work of the wave-induced momentum flux against the mean wind velocity gradient, and the energy loss due to the correlation of the turbulent stress and the gradient of the wave-induced wind velocity.

The energy balance equation for the TKE is obtained by multiplying (A6) by u_i, averaging it (which results in the conservation equation for the total energy), and subtracting (A15). The TKE conservation equation reads

$$\frac{\partial}{\partial \xi_3}F^t + \tau_\alpha\frac{\partial U_\alpha}{\partial \xi_3} + \overline{\tilde{\tau}_{ij}\frac{\partial \tilde{u}_i}{\partial \xi_j}} - \text{Diss} = 0, \tag{A17}$$

where F^t is the vertical flux of the TKE, Diss is the TKE viscous dissipation, and the second and the third terms describe the production of the TKE by the mean and the wave-induced motion. Notice that the latter term describes the energy sink of the wave motion into the turbulence [the last term in (A15)]. Using (A15) the TKE balance equation can be written as

$$\frac{\partial}{\partial \xi_3}(F^t + F^w) + (\tau_\alpha + \tau_\alpha^w)\frac{\partial U_\alpha}{\partial \xi_3} - \text{Diss} = 0. \tag{A18}$$

c. Equations for a small wave-induced disturbance in the airflow

To obtain expressions for the surface energy and momentum flux, equations describing a small linear wave-induced variation in the airflow are needed. To the first order in wave slope ($AK \ll 1$) the linearized (A11) written in terms of the amplitude $\hat{y}$ (which is a complex variable) of the harmonic oscillation $\tilde{y} = \hat{y}\exp(iKx_1)$ are

$$iKU_1\hat{u}_1 + \hat{v}_3\frac{dU_1}{d\xi_3} = -iK\hat{p} + \frac{\partial \hat{\tau}_{13}}{\partial \xi_3} \quad \text{and} \tag{A19}$$

$$iKU_1\hat{u}_3 = -\frac{\partial \hat{p}}{\partial \xi_3}, \tag{A20}$$

where terms containing the normal component of the Reynolds stress are omitted [as it was argued by Kudryavtsev et at. (2001), their role is not important]. In AK order, the amplitude of the contravariant vertical velocity $\hat{v}_3$ in (A19) is $\hat{v}_3 = \hat{u}_3 + \xi_{3,1}U_1$. Correspondingly, in AK order the continuity equation [(A7)] reads

$$iK\hat{u}_1 + \frac{\partial \hat{v}_3}{\partial \xi_3} = \xi_{3,1,3}U_1, \tag{A21}$$

where $\xi_{3,1,3} = \partial^2\xi_3/\partial x_1\partial x_3$. Equations (A19), (A20), and (A21) describe the linear undulation of the turbulent airflow over the surface wave.

d. Attenuation/growth rate of surface waves

First, the attenuation/growth of waves due to the work of the surface stress against the wave orbital velocity described by the second term in (8) is considered. The amplitude of the wave-induced variation in the shear stress inside the IR $\hat{\tau}_1$ is given by Meirink et al. [2003, their (23)]. In present terms this equation reads (neglecting terms of the second order)

$$\hat{\tau}_{s1} = (1 + \cos^2\theta)\kappa b^{1/2}\varsigma\frac{\partial\hat{u}_1}{\partial\varsigma} \simeq (1 + \cos^2\theta)\kappa b^{1/2}\frac{\Delta\hat{u}_1}{\ln(l/\varsigma_0)}. \quad \text{(A22)}$$

The second equality results from an estimate $\partial\hat{u}_1/\partial\ln\varsigma \sim \Delta\hat{u}_1/\ln(l/\varsigma_0)$, where $\Delta\hat{u}_1$ is the drop of the wind velocity variation amplitude over the IR: $\Delta\hat{u}_1 = \hat{u}_1(l) - C$. The horizontal velocity variation in the OR is given by Kudryavtsev et al. (2001) as

$$\hat{u}_1(\varsigma) = U_1(\varsigma)\exp(-K\varsigma) + 2\int_\varsigma^\infty U_1' e^{-K\varsigma_1}\, d\varsigma_1,$$

$U_1(\varsigma) = \overline{u}_1(\varsigma) - C$, and the velocity drop in (A22) at small Kl can be expressed as

$$\Delta\hat{u}_1 \simeq U_l - C - 2\cos\theta\frac{u_*}{\kappa}\ln(Kl). \quad \text{(A23)}$$

Accounting for (A22) and (A23) the wave energy attenuation/growth rate is

$$\beta_\tau = \frac{\rho_\alpha\overline{\tilde{u}_s\tilde{\tau}_{s1}}}{\Omega E} = \frac{\rho_a}{\rho_w}(1 + \cos^2\theta)\left\{\cos\theta\left[1 - \frac{2\ln(Kl)}{\ln(l/\varsigma_0)}\right] - \frac{2C}{\overline{u}_l}\right\}\frac{\upsilon_*^2}{C^2}, \quad \text{(A24)}$$

where $E = \rho_w g A^2/2$ is the swell energy and $\overline{u}_l = \upsilon_*^2/(\kappa b^{1/2})\ln(l/\varsigma_0)$ is the wind speed at $\varsigma = l$ [see (20)].

The energy transfer due to the action of the wave slope correlated pressure is described by the first term in (8). The imaginary part of the amplitude of the surface pressure $\hat{p}_s$, which is responsible for the energy transfer, is found from (A20) integrated over height:

$$\mathrm{Im}(\hat{p}_s) = K\int_{z_0}^\infty \mathrm{Re}(\hat{u}_3)U_1\, d\varsigma \simeq \hat{w}_l U_K, \quad \text{(A25)}$$

where $U_K = U_1(K^{-1})$ and $\hat{w}_l$ is the real (elevation correlated) part of the vertical velocity at $\varsigma = l$. To obtain the estimate of $\mathrm{Im}(\hat{p}_s)$ the following conditions were accounted for: inside the OR, $\mathrm{Re}(\hat{u}_3)$ attenuates exponentially [i.e., $\mathrm{Re}(\hat{u}_3) \approx \hat{w}_l\exp(-K\varsigma)$; see Kudryavtsev et al. 2001, their (57)]; the pressure is approximately constant over the IR; and at small Kl the integral $K\int_l^\infty U_1\exp(-K\varsigma)d\varsigma$ can be approximated by U_K.

Inside the IR the profile of the real part of the vertical velocity is approximately linear over the height: $\mathrm{Re}(\hat{u}) \sim (\varsigma/l)w_l$. Assuming that the dynamics of the IR results from the balance between the advective term and the Reynolds shear stress terms, and that the pressure term does not play a dominant role, the real part of the vertical velocity on the top of the IR $\hat{w}_l$ follows from (A19) and (A21):

$$\hat{w}_l \sim \frac{\hat{\tau}_{s1}}{U_l - 2\upsilon_*/\kappa\cos\theta}, \quad \text{(A26)}$$

where $\hat{\tau}_{s1}$ is the real quantity defined by (A22) with (A23). For fast-propagating surface waves ($U_l \approx -C$) the estimate of the vertical velocity is

$$\hat{w}_l \sim 2(1 + \cos^2\theta)\ln^{-1}(l/\varsigma_0)b^{1/2}.$$

For waves propagating with the wind speed ($U_l \approx 0$),

$$\hat{w}_l \sim (1 + \cos^2\theta)b^{1/2},$$

and for slowly propagating waves [$U_l \approx \overline{u}_1(l)$] the vertical velocity is

$$\hat{w}_l \sim (1 + \cos^2\theta)\ln^{-1}(l/\varsigma_0)b^{1/2}.$$

Thus the real part of the vertical velocity attains the maximal magnitude in the vicinity of $U_l \approx 0$. This is consistent with the model calculations of Mastenbroek et al. (1996), Sullivan et al. (2000), and Kudryavtsev et al. (2001). For practical applications (A26) with (A22) is written as

$$\hat{w}_l = 2(1 + \cos^2\theta)b^{1/2}\ln^{-1}(l/\varsigma_0)\phi(Kl, \theta), \quad \text{(A27)}$$

where $\phi(Kl, \theta)$ is a correction function, which allows for all three above-mentioned asymptotes:

$$\phi(Kl, \theta) = 1 + c_p(Kl/\kappa)^2\ln(l/\varsigma_0) - \mathrm{sign}(U_l)Kl\ln(Kl)/\kappa^2\cos\theta/[(1 + \cos^2\theta)]. \quad \text{(A28)}$$

Here c_p is a tuning constant of order 1 chosen as $c_p = 2$ by fitting the analytical expression to the model calculations. Last, the dimensionless attenuation/growth rate due to the action of pressure on the wave slope is found from (A25) and (A27):

$$\beta_p = \frac{\rho_a C\overline{\tilde{p}_s z_1}}{\Omega E} = 2\frac{\rho_a}{\rho_w}(1 + \cos^2\theta)\phi(Kl, \theta)\frac{U_K}{\hat{u}_l}\frac{\upsilon_*^2}{C^2}. \quad \text{(A29)}$$

REFERENCES

Belcher, S. W., 1999: Wave growth by non-separated sheltering. *Eur. J. Mech.*, **18B,** 447–462.

——, and J. C. R. Hunt, 1993: Turbulent shear flow over slowly moving waves. *J. Fluid Mech.*, **251,** 109–148.

Cohen, J. E., and S. E. Belcher, 1999: Turbulent shear flow over fast-moving waves. *J. Fluid Mech.*, **386,** 345–371.

Davidson, K. L., and A. K. Frank, 1973: Wave-related fluctuations in the airflow above natural waves. *J. Phys. Oceanogr.*, **3,** 102–119.

Donelan, M. A., 1999: Wind-induced growth and attenuation of lab-

oratory waves. *Wind-Over-Wave Couplings*, S. G. Sajjadi, N. H. Thomas, and J. C. R. Hunt, Eds., Calrendon Press, 183–194.
——, F. W. Dobson, S. D. Smith, and R. J. Anderson, 1993: On the dependence of sea surface roughness on wave development. *J. Phys. Oceanogr.,* **23,** 2143–2149.
——, W. M. Drennan, and K. B. Katsaros, 1997: The air–sea momentum flux in conditions of wind sea and swell. *J. Phys. Oceanogr.,* **27,** 2087–2099.
Drennan, W. M., H. C. Graber, and M. A. Donelan, 1999: Evidence for the effects of swell and unsteady winds on marine wind stress. *J. Phys. Oceanogr.,* **29,** 1853–1864.
Grachev, A. A., and C. W. Fairall, 2001: Upward momentum transfer in the marine boundary layer. *J. Phys. Oceanogr.,* **31,** 1698–1711.
Guo-Larsen, X., V. K. Makin, and A.-S. Smedman, 2003: Impact of waves on the sea drag: Measurements in the Baltic Sea and a model interpretation. *Global Atmos. Ocean Syst.,* **9,** 97–120.
Harris, D. L., 1966: The wind-driven wind. *J. Atmos. Sci.,* **23,** 688–693.
Kudryavtsev, V. N., and V. K. Makin, 2002: Coupled dynamics of short wind waves and air flow over long surface waves. *J. Geophys. Res.,* **107,** 3209, doi:10.1029/2001JC001251.
——, V. K. Makin, and J. F. Meirink, 2001: Simplified model of the air flow above waves. *Bound.-Layer Meteor.,* **100,** 63–90.
Maat, N., C. Kraan, and W. A. Oost, 1991: The roughness of the sea surface. *Bound.-Layer Meteor.,* **54,** 89–103.
Makin, V. K., and C. Mastenbroek, 1996: Impact of waves on air–sea exchange of sensible heat and momentum. *Bound.-Layer Meteor.,* **79,** 279–300.
——, and V. N. Kudryavtsev, 1999: Coupled sea surface–atmosphere model. 1. Wind over waves coupling. *J. Geophys. Res.,* **104,** 7613–7623.
——, and ——, 2002: Impact of dominant waves on sea drag. *Bound.-Layer Meteor.,* **103,** 83–99.
Mastenbroek, C., V. K. Makin, M. H. Garat, and J. P. Giovanangeli, 1996: Experimental evidence of the rapid distortion of turbulence in the air flow over water waves. *J. Fluid Mech.,* **318,** 273–302.
Meirink, J. F., V. N. Kudryavtsev, and V. K. Makin, 2003: Note on the growth rate of water waves propagating at an arbitrary angle to the wind. *Bound.-Layer Meteor.,* **106,** 171–183.
Plant, W. J., 1982: A relationship between wind stress and wave slope. *J. Geophys. Res.,* **87,** 1961–1967.
Smedman, A., U. Högström, H. Bergström, and A. Rutgersson, 1999: A case study of air–sea interaction during swell conditions. *J. Geophys. Res.,* **104,** 25 833–25 851.
Smith, S. D., and Coauthors, 1992: Sea surface wind stress and drag coefficients: The HEXOS results. *Bound.-Layer Meteor.,* **60,** 109–142.
Snodgrass, F. E., G. W. Groves, K. F. Hasselmann, G. R. Miller, W. H. Munk, and W. H. Powers, 1966: Propagation of ocean swell across the Pacific. *Philos. Trans. Roy. Soc. London,* **259A,** 431–497.
Sullivan, P. P., J. C. McWilliams, and C. H. Moeng, 2000: Simulation of turbulent flow over idealized water waves. *J. Fluid Mech.,* **404,** 47–85.
Townsend, A. A., 1972: Flow in a deep turbulent boundary layer over a surface distorted by water waves. *J. Fluid Mech.,* **55,** 719–735.
Yelland, M., and P. Taylor, 1996: Wind stress measurements from the open ocean. *J. Phys. Oceanogr.,* **26,** 541–558.